GEOPHYSICS, VOL. 68, NO. 5 (SEPTEMBER-OCTOBER 2003); P. 1569–1579, 12 FIGS., 2 TABLES.
10.1190/1.1620631

Pore pressure estimation in reservoir rocks from seismic reflection data

José M. Carcione*, Hans B. Helle‡, Nam H. Pham**, and Tommy Toverud§

ABSTRACT

A method is used to obtain pore pressure in shaly sandstones based upon an acoustic model for seismic velocity versus clay content and effective pressure. Calibration of the model requires log data—porosity, clay content, and sonic velocities—to obtain the dry-rock moduli and the effective stress coefficients as a function of depth and pore pressure. The seismic P-wave velocity, derived from reflection tomography, is fitted to the theoretical velocity by using pore pressure as the fitting parameter. This approach, based on a rock-physics model, is an improvement over existing pore-pressure prediction methods, which mainly rely on empirical relations between velocity and pressure. The method is applied to the Tune field in the Viking Graben sedimentary basin of the North Sea. We have obtained a high-resolution velocity map that reveals the sensitivity to pore pressure and fluid saturation in the Tarbert reservoir. The velocity map of the Tarbert reservoir and the inverted pressure distribution agree with the structural features of the Tarbert Formation and its known pressure compartments.

INTRODUCTION

Knowledge of pore pressure using seismic data helps in planning the drilling process—that is, casing and mud-weight design—to control potentially dangerous abnormal pressures. Proper pore-pressure prediction should involve the drilling engineer, the geologist, the geophysicist, and the petrophysicist, since the procedure requires mud-weight information, knowledge of the tectonic features of the area, use of seismic and well data, and determination of petrophysical parameters relevant to the problem.

Let us introduce some useful definitions about the different pressures considered in this work. Pore pressure, also known as formation pressure, is the in-situ pressure of the fluids in the pores. The pore pressure is equal to the hydrostatic pressure when the pore fluids support the weight of only the overlying pore fluids (mainly water). The lithostatic or confining pressure results from the weight of overlying sediments, including the pore fluids. When the pore pressure attains the lithostatic pressure, the fluids support all of the weight. However, fractures perpendicular to the minimum compressive stress direction appear for a given pore pressure, typically 70–90% of the confining pressure. When fracturing occurs, the fluid escapes from the pores and pore pressure decreases. In addition, pore pressure can decrease as a result of the presence of horizontal permeability, which may prevent the development of overpressures. In normally pressured sedimentary basins, the effect of a high sedimentation rate can be counteracted by horizontal permeability effects and prevent compaction disequilibrium.

A rock is said to be overpressured when its pore pressure is significantly greater than hydrostatic pressure. The difference between confining and pore pressures is called differential pressure. Acoustic and transport properties of rocks generally depend on effective pressure, a combination of pore and confining pressures [see equation (3)]. Various physical processes cause anomalous pressures on an underground fluid. The most common causes of overpressure are compaction disequilibrium and cracking, i.e., oil-to-gas conversion (Mann and Mackenzie, 1990; Luo and Vasseur, 1996).

In general, nonseismic methods to predict pore pressure are based on a relation between porosity or void ratio and effective stress (Bryant, 1989; Holbrook et al., 1995; Audet, 1996; Traugott, 1997). Indirect use of velocity information involves estimating of the porosity profile by using sonic-log data (Hart et al., 1995; Harrold et al., 1999). A measurement while drilling (MWD) technique is proposed by Lesso and Burgess (1986), based on mechanical drilling data [rock strength computed from rate of penetration (ROP), weight on bit (WOB), and torque (TOR)] and gamma-ray logs. Seismic data can be used to predict abnormal pore pressures in advance of

Manuscript received by the Editor April 5, 2002; revised manuscript received January 27, 2003.
*Istituto Nazionale di Oceanografia e di Geofisica Sperimentale (OGS), Borgo Grotta Gigante 42c, 34010 Sgonico, Trieste, Italy. E-mail: jcarcione@ogs.trieste.it.
‡Norsk Hydro ASA, E&P Research Centre, Sandsliveien 90, N-5020 Bergen, Norway. E-mail: hans.b.helle@nho.hydro.com.
**Formerly Norwegian University of Science and Technology, Department of Petroleum Engineering and Applied Geophysics, N-7491 Trondheim, Norway; presently Statoil ASA, N-7501 Stjørdal, Norway. E-mail: namhp@statoil.com.
§Formerly Altinex ASA, N-5061 Kokstad, Norway; presently Norwegian University of Science and Technology, Department of Petroleum Engineering and Applied Geophysics, N-7491 Trondheim, Norway. E-mail: tommyt@ipt.ntnu.no.

drilling. In general, this prediction has been based on empirical models relating pore pressure to sonic and/or seismic velocity (Pennebaker, 1968; Eaton, 1972; Belotti and Giacca, 1978; Bilgeri and Ademeno, 1982; Dutta and Levin, 1990; Kan and Sicking, 1994; Bowers, 1995; Eaton and Eaton, 1997; Sayers et al., 2000).

Unlike previous theories, we use a Biot-type three-phase theory that considers the existence of two solids (sand grains and clay particles) and a fluid. The theory, developed by Carcione et al. (2000), is generalized here to include the effects of pore and confining pressure to estimate pore pressure from seismic velocities. At low frequencies, this theory is a generalization of Gassmann's equation for shaly sandstones, based on first physical principles. The theory was verified using real measurements of compressional and shear-wave velocities versus porosity and clay content. The model predicts additional slow waves, but they are not used for pressure prediction. Attenuation from mode conversion and other mechanisms is neglected. The method requires high-resolution velocity information, preferably obtained from seismic inversion techniques. As is well known, interval velocities obtained from conventional seismic processing are not reliable enough for accurate pore-pressure prediction (Sayers et al., 2000; Carcione and Tinivella, 2001). Calibration of the model requires well information, that is, porosity and shale volume estimation, direct measurements of pore pressure, and sonic-log data. Laboratory measurements of P- and S-wave velocities on core samples may further improve the calibration process (Carcione and Gangi, 2000a,b).

PORE-PRESSURE PREDICTION METHOD

The sand–clay acoustic model for shaly sandstones developed by Carcione et al. (2000) yields the seismic velocities as a function of clay (shale) content, porosity, saturation, dry-rock moduli, and fluid and solid-grain properties. As stated in previous works (Carcione and Gangi, 2000a,b), variations in seismic velocity are mainly because the dry-rock moduli are sensitive functions of the effective pressure, with the largest changes occurring at low differential pressures. Explicit changes in porosity and saturation are important but have a lesser influence on wave velocities than changes in the moduli. This is because the moduli are highly affected by the contact stiffnesses between grains. In this sense, porosity-based methods can be highly unreliable. In fact, variations of porosity for Navajo Sandstone, Weber Sandstone, and Berea Sandstone are only 1.7%, 7%, and 4.5%, respectively, for changes of the confining pressure from 0 to 100 MPa (Berryman, 1992).

To use the present theory to predict pore pressure, we need to obtain the expression of the dry-rock moduli versus effective pressure. The calibration process should be based on well, geological, and laboratory data—mainly sonic and density data—and porosity and clay content inferred from logging profiles.

Let us assume a rock at depth z. The lithostatic or confining pressure p_c can be obtained by integrating the density log. We know that

$$p_c = g\int_0^z \rho(z')dz', \tag{1}$$

where ρ is the density and g is the acceleration of gravity. Furthermore, the hydrostatic pore pressure p_H is approximately given by

$$p_H = \rho_w g z, \tag{2}$$

where ρ_w is the density of water.

As a good approximation (Prasad and Manghnani, 1997), compressional- and shear-wave velocities and compression and shear moduli depend on effective pressure p_e:

$$p_e = p_c - np, \tag{3}$$

where p is pore pressure and n is the effective stress coefficient, which can be different for velocities and moduli (Christensen and Wang, 1985). Note that the effective pressure equals the confining pressure at zero pore pressure. We find that $n \approx 1$ for static measurements of the compressibilities (Zimmerman, 1991), while n is approximately linearly dependent on the differential pressure $p_d = p_c - p$ in dynamic experiments (Gangi and Carlson, 1996; Prasad and Manghnani, 1997). Therefore, we assume

$$n = n_1 - n_2 p_d = n_1 - n_2(p_c - p). \tag{4}$$

This dependence of n versus differential pressure is in good agreement with the experimental values corresponding to the compressional velocity obtained by Christensen and Wang (1985) and Prasad and Manghnani (1997). Clearly to obtain n_1 and n_2 we need two evaluations of n at different pore pressures, preferably a normally pressured well and an overpressured well. Alternatively, n_1 can be assumed equal to 1, and only one evaluation is necessary in this case.

Calibration of the model

Ideally, a precise determination of n requires laboratory experiments on saturated samples for different confining and pore pressures. However, even this laboratory n does not reflect the behavior of the rock at in-situ conditions for two main reasons. First, laboratory measurements of wave velocity are performed at ultrasonic frequencies Second, the in-situ stress distribution is different from the stress applied in the experiments.

No laboratory experiments available.—In the absence of laboratory data, or for shales, we perform the following steps with the data available from a calibration well.

First, we consider the model of Krief et al. (1990) to obtain an estimate of the dry-rock moduli K_{sm}, μ_{sm} (sand matrix), K_{cm}, and μ_{cm} (clay matrix) versus porosity and clay content. The porosity dependence of the sand and clay matrices should be consistent with the concept of critical porosity (Mavko et al., 1998, p. 244) since the moduli should vanish above a certain value of the porosity (usually from 0.4 to 0.5). This dependence is determined by the empirical coefficient A [see equation (5)]. This relation is suggested by Krief et al. (1990) and is applied to sand–clay mixtures by Goldberg and Gurevich (1998). The bulk and shear moduli of the sand and clay matrices are given by, respectively,

$$K_{sm}(z) = K_s[1 - C(z)][1 - \phi(z)]^{1+A/[1-\phi(z)]},$$
$$K_{cm}(z) = K_c C(z)[1 - \phi(z)]^{1+A/[1-\phi(z)]},$$

$$\mu_{sm}(z) = \frac{K_{sm}(z)\mu_s}{K_s},$$
$$\mu_{cm}(z) = \frac{K_{cm}(z)\mu_c}{K_c}, \tag{5}$$

where K_s and μ_s are the bulk and shear moduli of the sand grains and where K_c and μ_c those of the clay particles. Krief et al. (1990) set the A parameter to three regardless of the lithology, and Goldberg and Gurevich (1998) obtain values between two and four, while Carcione et al. (2000) use two. Alternatively, the value of A can be estimated by using regional data from the study area. We use a general form of Goldberg and Gurevich's equation. Experimental data are fitted in Carcione et al. (2000), showing that the model has been tested successfully. The model is not based on a dual porosity theory; rather, there is only one (connected) porosity. The clay moduli are taken from fit to experimental data in Goldberg and Gurevich's paper.

Second, we assume the following functional form for the dry-rock moduli as a function of effective pressure:

$$M(z) = \alpha(z)[1 - \exp(-p_e/p^*(z))], \tag{6}$$

where $\alpha(z)$ and $p^*(z)$ are parameters that should be obtained (for each moduli) by fitting Krief et al.'s expressions (5). Initially, we assume that the effective pressure at depth z is $p_e = p_c - p$ (Zimmerman, 1991, p. 43; Carcione, 2001, p. 233), where p_c is given by equation (1) and p are taken from the formation pressure data in the calibration wells (see Figure 7). Since there are two unknown parameters (α and p^*) and one value of M for each depth, $\alpha(z)$ is assumed to be equal to the Hashin-Shtrikman (HS) upper bounds (Hashin and Shtrikman, 1963; Mavko et al., 1998, p. 106):

$$K_{\mathrm{HS}}(z) = \left\{K_s + \phi(z)\left[(1-\phi(z))\left(K_s + \frac{4}{3}\mu_s\right)^{-1} - K_s^{-1}\right]^{-1}\right\} \tag{7}$$

and

$$\mu_{\mathrm{HS}}(z) = \mu_s\left\{1 + 5\phi(z)\left[2(1-\phi(z))(K_s + 2\mu_s) \times \left(K_s + \frac{4}{3}\mu_s\right)^{-1} - 5\right]^{-1}\right\}. \tag{8}$$

Note that the HS lower bounds are zero and that the Voigt bounds are $(1-\phi)K_s$ and $(1-\phi)\mu_s$, respectively. For quartz grains with clay, $K_s = 39$ GPa and $\mu_s = 33$ GPa (Mavko et al., 1998, p. 307). If the limit porosity is 0.2, the HS upper bounds for the bulk and shear moduli are 26 and 22 GPa, compared to the Voigt upper bounds of 31 and 26 GPa, respectively. However, the HS bounds are still too large to model the moduli of in-situ rocks. These contain clay and residual water saturation, inducing a chemical weakening of the contacts between grains (Knight and Dvorkin, 1992; Mavko et al., 1998, p. 203). Figure 1 shows the dry-rock bulk modulus of several reservoir rocks for different confining pressures (Zimmerman, 1991, p. 29, Table 3.1), compared to the HS upper bounds. The solid line represents the analytical curve (9). On the basis of these data points, we apply a constant weight factor $\beta = 0.8$ to the HS bounds, a result of the softening effects.

Third, we compute the exponential coefficients [see equation (6)] using the values of the moduli obtained in step one, the confining and (measured) pore pressures, and the effective stress coefficients equal to one. For instance, equation (6) for the sand matrix can be written as

$$K_{sm}(z) = \beta K_{\mathrm{HS}}\left[1 - \exp\left(-p_e \big/ p_K^*(z)\right)\right] \tag{9}$$

and

$$\mu_{sm}(z) = \beta \mu_{\mathrm{HS}}\left[1 - \exp\left(-p_e / p_\mu^*(z)\right)\right]. \tag{10}$$

Thus,

$$p_K^*(z) = -p_e(z)\{\ln[1 - K_{sm}(z)/(\beta K_{\mathrm{HS}}(z))]\}^{-1} \tag{11}$$

and

$$p_\mu^*(z) = -p_e(z)\{\ln[1 - \mu_{sm}(z)/(\beta \mu_{\mathrm{HS}}(z))]\}^{-1}, \tag{12}$$

where we assume the effective pressure is equal to the differential pressure.

Let us estimate the error in determining p_K^*. Partial differentiation of p_K^* with respect to K_{sm} and p_e implies that the error in the determination of p_K^* is

$$\Delta p_K^* = \frac{p_K^*}{p_e}\left(\frac{p_K^* \Delta K_{sm}}{K_{\mathrm{HS}} - K_{sm}} + \Delta p_e\right), \tag{13}$$

where ΔK_{sm} and Δp_e are the errors corresponding to K_{sm} and p_e, respectively. Consider the following example: $K_{\mathrm{HS}} = 30$ GPa, $\Delta K_{sm} = 1$ GPa, and $\Delta p_e = 1$ MPa. For $p_K^* = 15$ MPa (soft rock), the error is 4.5 MPa at $p_e = 50$ MPa and 20 MPa at $p_e = 5$ MPa; while for $p_K^* = 40$ MPa (stiff rock), the error is 4.5 MPa at $p_e = 50$ MPa and 5.1 MPa at $p_e = 5$ MPa. Therefore, the analysis indicates that a better estimation of p_K^* is achieved at high effective pressures and stiff rocks, that is, using data from normally pressured wells.

The last step of the calibration process is to consider equation (3) and obtain the effective stress coefficients $n_K(z)$ and $n_\mu(z)$ by fitting the theoretical velocities (Carcione et al., 2000) to the corresponding sonic-log P-wave and S-wave velocities by

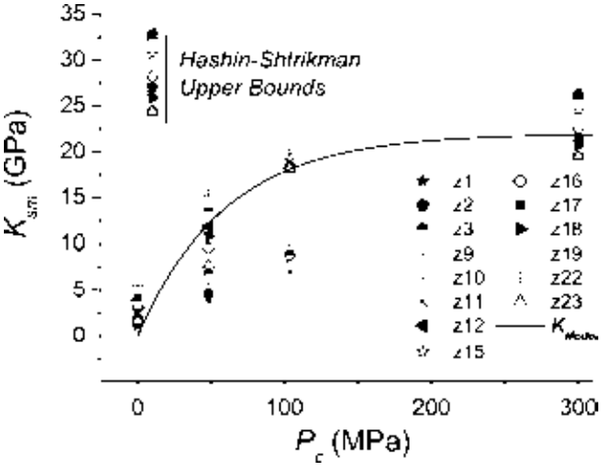

FIG. 1. Dry-rock bulk modulus of several reservoir rocks for different confining pressure, compared to the HS upper bounds. The solid line represents the analytical curve equation (9). The data are taken from Zimmerman (1991, Table 3.1).

using expressions (6). First, we obtain n_μ by fitting the S-wave velocity because this velocity only depends on μ_{sm}. Then we obtain n_K by fitting the P-wave velocity. If shear-wave velocity data are unavailable, we assume $n_\mu = 1$. From the values of n obtained at the two wells, we obtain the linear law (4) for the geological unit under investigation. The values of clay content and porosity away from the wells are assumed to be equal to those of the nearest well. Interpretation is required to follow the geological units laterally, as a function of depth, so the n profiles can be properly extrapolated. In this study, the clay-matrix moduli K_{cm} and μ_{cm} are given by Krief et al.'s equations (5), with no explicit dependence on pressure.

Note that the HS bounds do not depend on the size and shape of the grain and pores. In this sense, the model has a general character. The only conditions are linearity, isotropy, and the low-frequency approximation.

More precisely, we use the following data of the study area to calibrate the model and obtain the effective stress coefficient profile for the formations under consideration:

1) an estimate of the porosity profile $\phi(z)$ to use in Krief et al.'s model (see below) and in the sand–clay acoustic model (from a series of logs using artificial neural networks; Helle et al., 2001, and Helle and Bhatt, 2002,

2) an estimate of the clay-content profile $C(z)$ to use in Krief et al.'s model (see below) and in the sand–clay acoustic model (shale volumes obtained from SP logs or gamma-ray logs or using neural networks; Helle et al., 2001, and Helle and Bhatt, 2002,

3) direct measurements of pore pressure $p(z)$ from repeat formation tests and/or mud weights provided by the mud-logging operator, and

4) sonic-log information, that is, the P- and S-wave velocity profiles $V_P(z)$ and $V_S(z)$ used to obtain n_K and n_μ for the whole range of effective pressures by fitting the theoretical wave velocities to V_P and V_S, where n_K and n_μ are the effective stress coefficients corresponding to the dry-rock bulk and shear moduli, respectively.

Laboratory experiments available.—The evaluation can be improved if laboratory data of dry-rock P- and S-wave velocities are available; this serves to constrain the values of α and p^* in equation (6). These sparse calibration points are based on sandstone or shaly sandstone cores, since dry measurements in shals are practically impossible to perform. If sandstone cores are available, we proceed as follows.

The upper limits (infinite confining pressure) and exponential coefficients of the moduli are obtained by fitting the dry-rock moduli, which are calculated from the dry-rock wave velocities, while n is obtained from experiments on saturated samples for different confining and pore pressures (Carcione and Gangi, 2000a,b).

The seismic bulk moduli K_{sm} and μ_{sm} versus confining pressure can be obtained from laboratory measurements in dry samples. If $V_P(\text{dry})$ and $V_S(\text{dry})$ are the experimental compressional and shear velocities, the moduli are given approximately by

$$K_{sm} = (1-\phi)\rho_s\left(V_P(\text{dry})^2 - \frac{4}{3}V_S(\text{dry})^2\right)$$

and

$$\mu_{sm} = (1-\phi)\rho_s V_S(\text{dry})^2, \qquad (14)$$

where ρ_s is the grain density. We recall that K_{sm} is the rock modulus at constant pore pressure, i.e., the case when the bulk modulus of the pore fluid is negligible compared with the dry-rock bulk modulus, as, for example, air at room conditions. Then, we perform experiments on saturated samples for different confining and pore pressures to obtain the effective stress coefficient n. Because these experiments yield the P- and S-wave velocities and because the effective stress coefficients of wave velocity and wave moduli may differ from each other, we obtain n for

$$K = \rho\left(V_P^2 - \frac{4}{3}V_S^2\right) \quad \text{and} \quad \mu = \rho V_S^2, \qquad (15)$$

where K and μ are the undrained moduli.

We continue with the last step of the preceding list. This step should improve the determination of n, estimated with laboratory experiments in the first step.

Pore-pressure calculation

Finally, the seismic velocity, derived from velocity analysis and inversion techniques, can be fitted with the theoretical velocities by using pore pressure as a fitting parameter. The theory (Carcione et al., 2000) allows us to introduce different kinds of information explicitly, such as composition (clay content), fluid saturation, porosity, permeability, and viscosity. Before dealing with the seismic data, we should test the above procedure in a nearby overpressured well. The pore pressure prediction flow chart is shown in Figure 2.

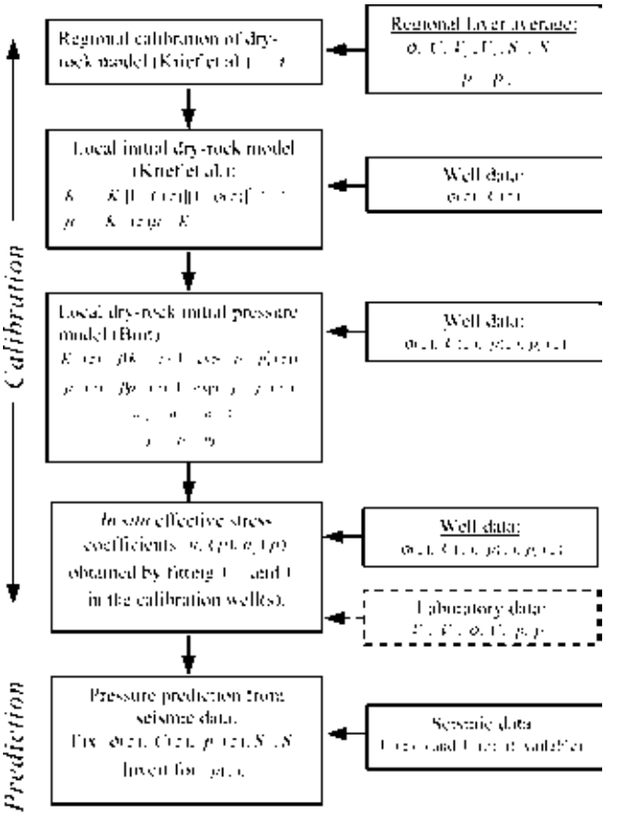

FIG. 2. Flowchart illustrating the pore-pressure prediction method from seismic data.

AVO-based verification.—In some cases, velocity information alone is not enough to distinguish between a velocity inversion resulting from overpressure and a velocity inversion from pore fluid and lithology [e.g., base-of-salt reflections (Miley, 1999; Miley and Kessinger, 1999)]. Occasionally, overpressuring is not associated with large velocity variations, as in smectite/illite transformations. Best et al. (1990) use AVO analysis to treat these cases. Modeling analysis of AVO signatures of pressure transition zones is given in Miley (1999), Miley and Kessinger (1999), and Carcione (2001). This type of analysis should complement the present prediction method on the basis of geological information of the study area.

EXAMPLE

We consider the Tune field area in the Viking Graben of the North Sea (Figure 3). This basin is 170–200 km wide and represents a fault-bounded, north-trending zone of extended crust, flanked by the mainland of western Norway and the Shetland platform. The area is characterized by large normal faults with north, northeast, and northwest orientations that define tilted blocks. Such blocks contain the sequences present within the well used for this study. The main motivation for selecting this area is that highly overpressured compartments were identified by drilling and higher overpressure is expected in future wells down the flank side toward the west into the central Viking Graben. A general overview of the petroleum geology of the North Sea can be found in Glennie (1998), and a detailed analysis of the fault sealing and pressure distribution in the Tune field is given by Childs et al. (2002).

Figure 4 displays the simplified stratigraphic table, where the geological ages of the main stratigraphic boundaries are indicated. The Tune field is essentially a gas reservoir with a thin layer of oil at its base. The reservoir is confined to the Tarbert Formation, located in the upper section of the Jurassic Brent Group, bounded by the shaly Heather Formation at the top (seal) and by the Ness Formation below.

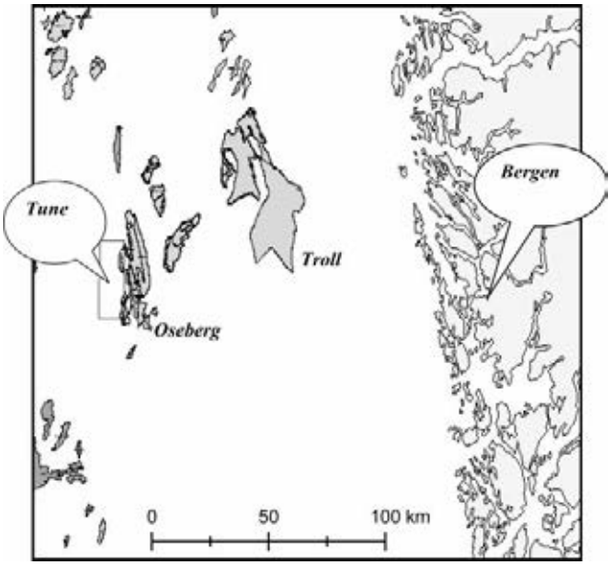

FIG. 3. Location of the Tune field in the Norwegian sector of the North Sea, offshore western Norway.

Figure 5 displays the time–structure map of the top Ness, showing faulting at a range of scales and orientations. On the western flank the reservoir terminates by a large fault plane where the entire Brent is downfaulted by several hundred meters. Within the field a major southwest–northeast dip-slip fault divides the Tarbert sand into two main compartments. This fault is expected to be crucial for sustaining the pressure differences in the field. Pressure data from wells on either side of the fault clearly indicate that the fault is a flow barrier, with a jump in pressure across the fault of 16 MPa. Wells 2 and 3 in the downfaulted compartment (Figure 6) in the north are overpressured (by about 15 MPa), and well 1 in the east compartment has almost normal (hydrostatic) pore pressure. The calibration well (well 1) is an exploration well drilled to a depth of 3720 m (driller's depth) to test the hydrocarbon potential of the Jurassic Brent Group. The well includes reservoir rocks of the Tarbert and Ness Formations, of which the Tarbert sands are the target unit considered in the present study. A Krief et al.'s parameter $A = 3.15$ is obtained by fitting sonic-log data.

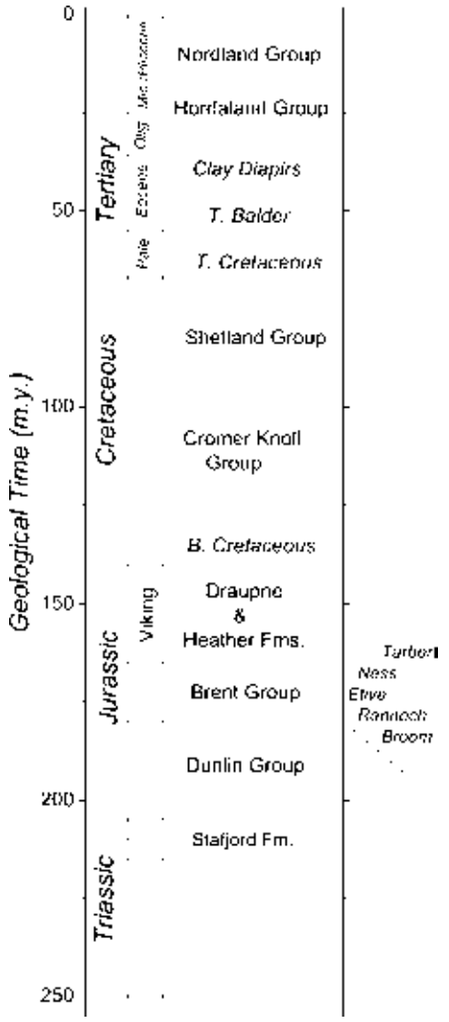

FIG. 4. Stratigraphic table of the northern North Sea, showing the main stratigraphic boundaries. The target unit for this study is the Tarbert Formation of the Jurassic Brent Group. For geological details see Glennie (1998).

The 3D marine seismic data were acquired by using a system of six 3-km-long streamers with a group interval of 12.5 m and cross-line separation of 100 m. The shot spacing was 25 m, and the sampling rate 2 ms. The conventional stacked section is displayed in Figure 6, where the location of the wells is shown. Figure 7 shows pressure and formation data for the Tune wells. The shear-wave velocity in well 3 is obtained by using the empirical relation $V_S = -791.75 + 0.76535\ V_P$ (m/s), obtained by fitting data from nearby wells. Note that well 1 is water bearing with almost normal pore pressures, while wells 2 and 3 are gas bearing and overpressured.

Velocity determination by tomography of depth-migrated gathers

Recent advances in depth migration have improved subsurface model determination based on reflection seismology.

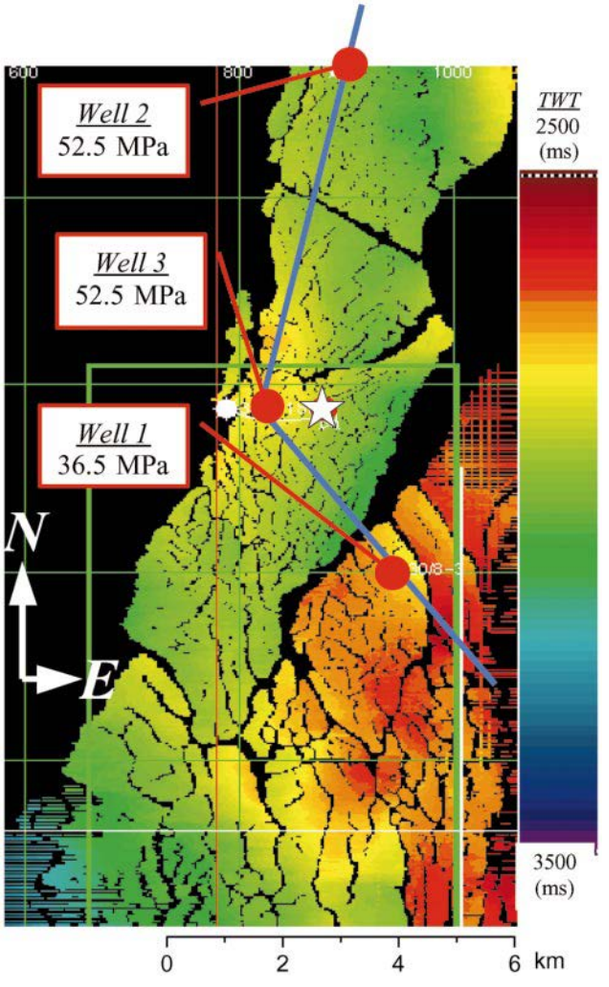

FIG. 5. Time–structure map of top Ness (base reservoir), showing the pressure compartments in the study area. Wells 2 and 3 are overpressured (by about 15 MPa). In Well 1 there is almost normal (hydrostatic) pore pressure. The blue line indicates the location of the seismic section shown in Figure 6. Notice that well 3 is highly deviated, as indicated by the well location at surface (white star) and at total depth (white bullet).

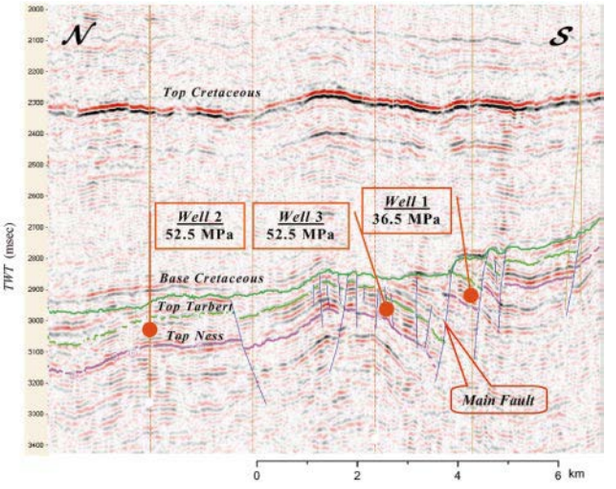

FIG. 6. Seismic section through Tune wells (Figure 5), showing the location of the top Tarbert–top Ness interval. The mean reservoir fluid pressures are indicated. The depths of interest are between top Tarbert (green) and top Ness (pink).

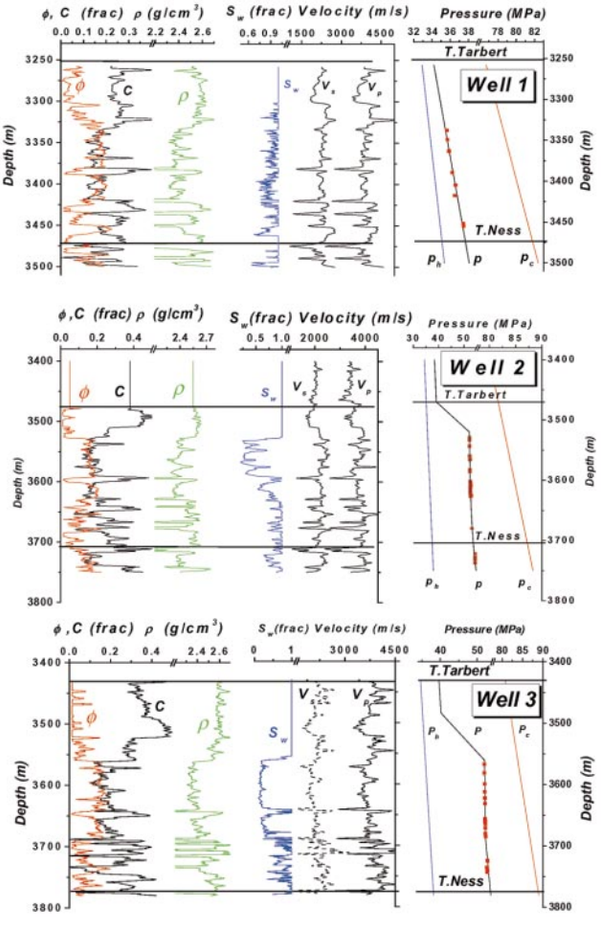

FIG. 7. Pressure and formation data: porosity ϕ, clay content C, density ρ, water saturation S_w, and sonic-log velocities V_P and V_S for the Tune wells (see Figures 5 and 6 for location).

Subsurface imaging is linked to velocity, and an acceptable image can be obtained only with a highly accurate velocity field. It has been recognized that prestack migration is a powerful velocity analysis tool that yields better imaging results than poststack migration in complicated structures. The basic assumption underlying the velocity determination methods based on prestack migration is that when the velocity is correct, all of the migrations with data in different domains (e.g., different offset, different shots, different migration angles, etc.) must yield a consistent image.

To obtain the velocity field, we use the seismic inversion algorithm described by Koren et al. (1998). Figure 8 shows the flow chart of the velocity analysis procedure. We start with an initial model based on the depth-converted time model, using a layer velocity cube based on conventional stacking velocities and the interpreted time horizons from the Tune project. Line by line, we perform the 3D prestack depth migration using the initial velocity model and an appropriate aperture (3×3 km at 3 km depth) in the 3D cube covering an area of about 7×20 km. Through several iteration loops the model is gradually refined in velocity and hence depth. Each loop includes reinterpretation of the horizons in the depth domain, residual moveout analysis, and residual moveout picks in the semblance volume. This is performed for each reflector of significance, starting at the seabed and successively stripping the layers down to the target. The tomography considers (1) an initial velocity model and (2) the errors as expressed by the depth gather residual moveout and the associated 3D residual maps. From these two inputs a new velocity model is derived where the layer depths and layer velocities are updated iteratively to yield flat gathers. The refined model is derived using a tomographic algorithm that establishes a link between perturbation in velocity and interface location, and traveltime errors along the common reflection point (CRP) rays traced across the model. CRP rays are ray pairs that obey Snell's law and emanate from points along the reflecting horizon, arriving at the surface with predefined offsets corresponding to the offset locations for the migrated gathers. Each pair establishes a relationship between the CRP and the midpoint of the rays at the surface. Depth errors, indicating the difference in depth of layer images and reference depth, are picked on the migrated gather along the horizon and converted to time errors along the CRP rays.

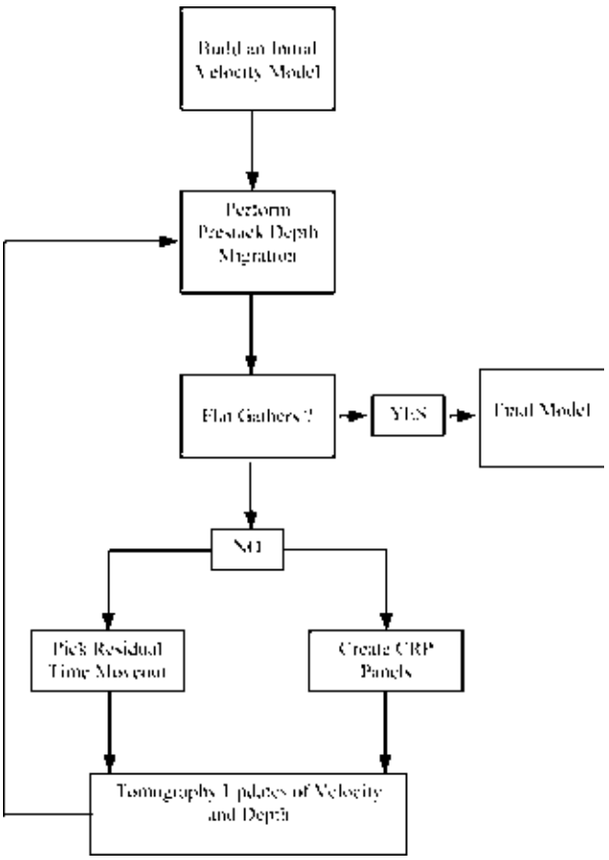

FIG. 8. Reflection tomography flowchart.

In this study we use a layer-based tomography, where the subsurface is described by a network of interlocking closed bodies best thought of as polygons rather than layers. Within each polygon the velocity is represented by a laterally continuous function, while velocity changes discontinuously across the polygon interface. Polygon velocities and thicknesses are updated in successive tomographic iterations. The objective is to find both the interface locations and the lateral velocity function within each polygon, which yields the flattest reflections in prestack migrated gathers (Kosloff et al., 1996). Layer-based tomography makes use of the structural framework as a constraint for interpolating velocity from one analysis point to the other. In the present situation, where velocities vary much less within the layers than between them, this framework is an effective constraint on interpolation. The equations relating the time errors to changes in the model are solved by a weighted least-squares technique.

The final model consists of seven layers (see Figure 4), i.e., the seawater layer, seabed–top diapir (clay diapirism is a characteristic feature of Tertiary throughout the area), top diapir–top Balder, top Balder–top Cretaceous, top Cretaceous–base Cretaceous, base Cretaceous–top Tarbert, and the target layer, top Tarbert–top Ness. Figure 9 shows the in-line (left) and crossline (right) velocity models, intersecting the gas-bearing high-pressure well 3.

The velocity maps for base Cretaceous (representing the velocity of the layer between top Cretaceous and base Cretaceous), top Tarbert (representing the layer between base Cretaceous and top Tarbert), and top Ness (representing the layer between top Tarbert and top Ness) are shown in Figure 10, where the well locations are indicated. This naming convention has been adopted because the seismic analysis focuses on CRP points at the base of the actual layer while the tomographic velocities are those of the rocks between base and top.

The Cretaceous layer velocity and the depth to base Cretaceous (not shown) reveal a remarkable similarity, i.e., where the Cretaceous is deep, the velocity is high; where the Cretaceous is shallow, the velocity is low, indicating the velocity of Cretaceous is essentially governed by the overburden (e.g., compaction). Whereas the structural features above the Cretaceous are fairly smooth, the geometry at base Cretaceous and below is more dramatic, as is apparent from the seismic section (Figure 6). In the northwest flank the Tarbert and Ness Formations terminate against the regional fault plane. Also, along the most significant local fault planes, the layers are undefined, and hence the discontinuity in the velocity maps. Structural

features are well displayed in the velocity maps of the top Tarbert and top Ness. However, the top Tarbert velocity map reveals a fairly scattered distribution, with small patches of highs and lows within the main fault blocks. For the reservoir itself, represented by the top Ness velocity map, the distribution is far more coherent. In the Tarbert Formation at wells 2 and 3 in the north fault block, velocities are consistently lower than at well 1 in the east block. This feature is pronounced, with a velocity increase of about 200 m/s across the fault separating the gas-bearing reservoir in the north block from the water-bearing reservoir in the east block. A high-velocity ridge separates the lows at wells 2 and 3. Distinct low-velocity zones are also seen to the south and southeast that are not correlated with the depth variations. On the other hand, the high-velocity zones in the southwest may be related to the Tarbert dipping down at the western flank. Table 1 shows the results of seven independent velocity analyses obtained at the three well locations, each analysis starting from a perturbed initial

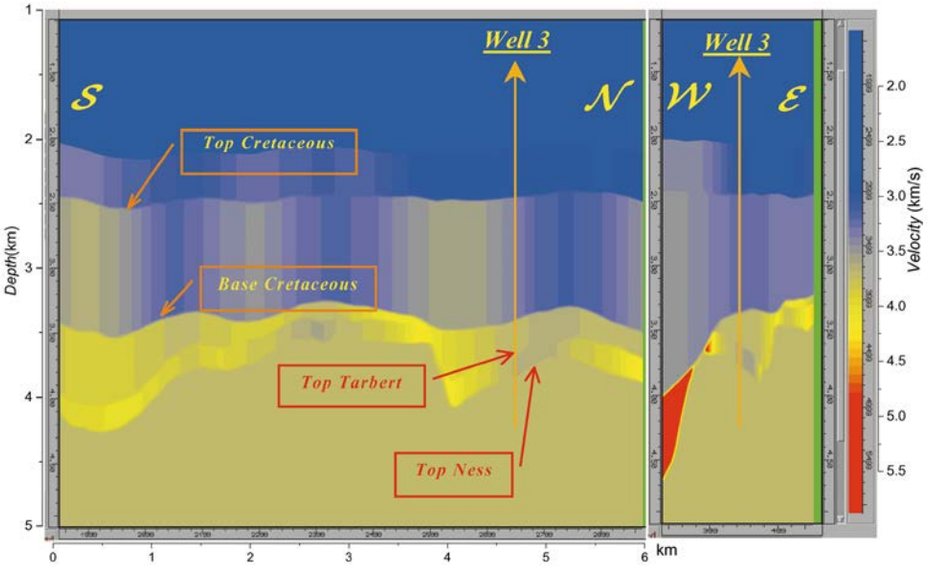

FIG. 9. In-line (left) and cross-line (right) velocity models, intersecting the gas-bearing high-pressured well 3.

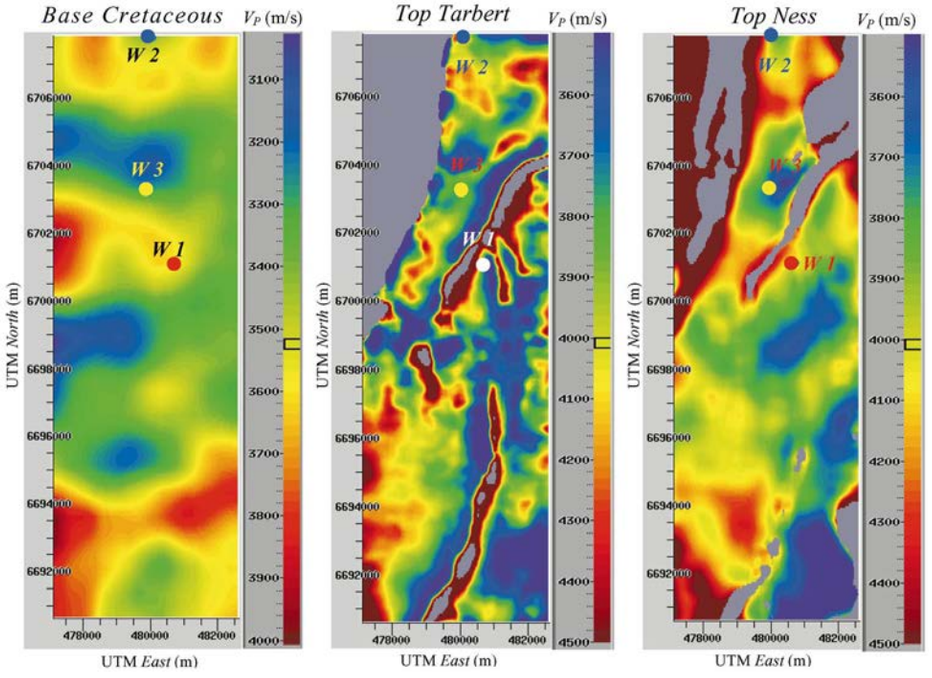

FIG. 10. Velocity maps for base Cretaceous to top Ness layers with individual color scale given in meters per second. Map axes annotations are the universal transverse mercator (UTM) grid coordinates (in meters). The velocity map represents the velocity of the layer between the given reflector and that above. The target for this study is the top Tarbert–top Ness layer (right).

velocity model. The standard deviation of 15 to 39 m/s indicates that errors in the tomographic velocity estimates are small compared with the lateral variation in the velocity field of about 200 m/s and are in fair agreement with the P-wave velocities obtained by averaging the sonic logs over the reservoir section (Figure 6).

Application of the velocity model for pressure prediction

To estimate the pressure map in the Tarbert Formation, we follow the procedure outlined above. Table 2 shows the values of the basic physical quantities used to compute the theoretical velocities. Gas density and gas bulk modulus are computed by using the van der Waals equation, as described in Carcione and Gangi (2000b). (The values indicated in the table are for hydrostatic pressure.) Figure 11 shows the effective stress coefficients as a function of differential pressure, obtained for wells 1 and 2. We assume that $n_1 = 1$, i.e., that at zero differential pressure the frame bulk modulus vanishes. The same assumption is used

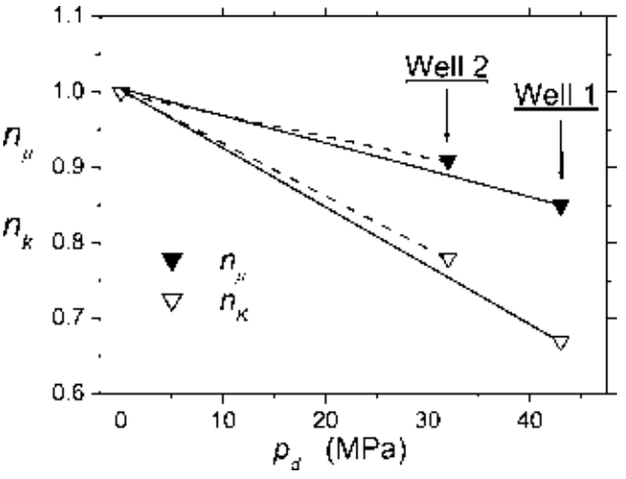

FIG. 11. Effective stress coefficients as a function of differential pressure p_d.

Table 1. Statistics of top Tarbert–top Ness tomography velocities at the well locations. Comparison with sonic velocities

Tomography	Well 1 (m/s)	Well 2 (m/s)	Well 3 (m/s)
1	4034	3883	3842
2	4025	3785	3825
3	4012	3777	3806
4	4004	3780	3791
5	3986	3797	3804
6	4012	3772	3803
7	4019	3782	3760
Mean, std.	4013, 15	3797, 39	3804, 26
Sonic *P*	3948	3735	3799
Sonic *S*	2246	2212	–

Table 2. Material properties

Material	Property
Sand	$\rho_s = 2650$ kg/m^3 $K_s = 39$ GPa $\mu_s = 33$ GPa
Clay	$\rho_c = 2650$ kg/m^3 $K_c = 20$ GPa $\mu_c = 10$ GPa
Pore fluids	$\rho_w = 1040$ kg/m^3 $K_w = 2.4$ GPa $\rho_g = 100$ kg/m^3 $K_g = 0.01$ GPa

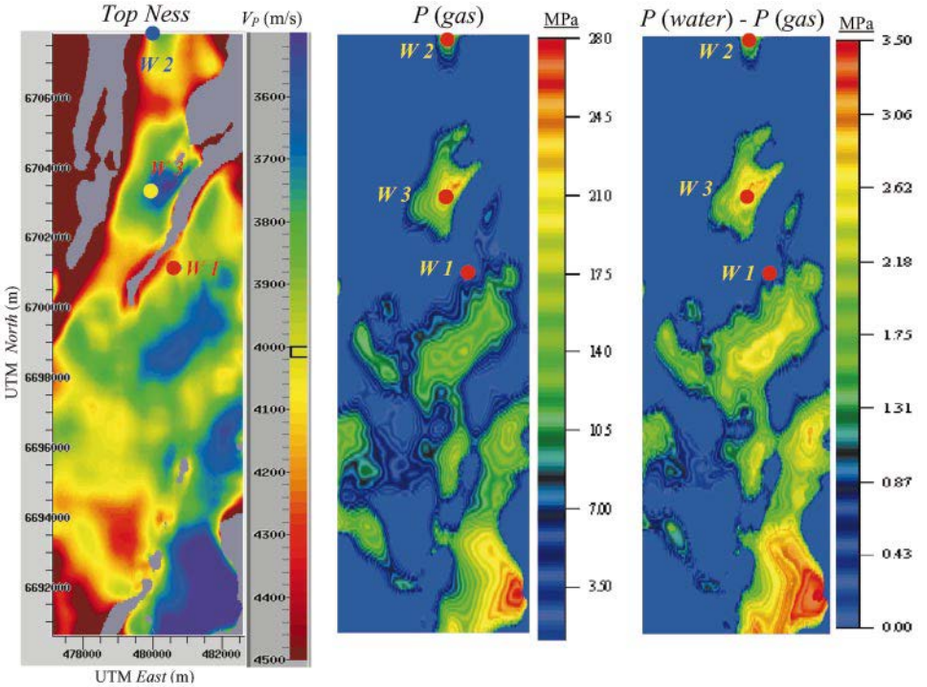

FIG. 12. Seismic velocity map (left, from Figure 10), overpressure prediction (center), and difference in overpressure resulting from water-bearing Tarbert and gas-bearing Tarbert (right).

for the effective stress coefficient related to the frame rigidity modulus.

Figure 12 shows the velocity map (left) and the overpressure map, assuming $S_w = 0.35$ and a gas saturation $S_g = 0.65$ (center). The picture at the right represents the difference in pore pressure by assuming gas-bearing Tarbert (center) and water-bearing Tarbert ($S_w = 0.94$ and $S_g = 0.06$). An overpressure of about 15 MPa is predicted for well 2, while slightly higher overpressure (18 MPa) is predicted for well 1. The direct measurements indicate overpressures of about 15 MPa (see Figure 7). Figure 12 (right) shows that the sensitivity of the model to fluid saturation is about 2.5 MPa. The results in Figure 12 support the hypothesis that the three wells are drilled in three isolated pressure compartments. Although the pressures in wells 2 and 3 are similar, the apparent high-velocity zone between those wells may indicate the existence of an isolated compartment with lower pressure. A closer inspection of the faults in Figures 5 and 6 may support this interpretation.

CONCLUSIONS

The velocity obtained by careful analysis of prestack 3D data from the deep and complex Tarbert reservoir in the Tune field is sufficiently sensitive to pressure and pore fluid to perform a meaningful analysis. The velocity and pressure distribution complies well with the structural features of the target and the general geological understanding of the pressure compartments in the Tune field. The partial saturation model used for pressure prediction can be calibrated conveniently against well data, provided that a complete set of logging data are available for the zone of interest. The most important part of the prediction process is determining the effective stress coefficients and dry-rock moduli versus effective pressure, since these properties characterize the acoustic behavior of the rock. The inversion method based on the shaly sandstone model must fix some parameters while inverting the others. For instance, assuming the reservoir and fluid properties (mainly, the saturation values), formation pressure can be inverted. Conversely, assuming the pore pressure, the saturations can be obtained. The latter implies that this method may be used in reservoir monitoring where the pressure distribution is known while saturation, i.e., the remaining hydrocarbon reserves, is uncertain.

The prediction method accounts for most of the causes of velocity variation, i.e., saturation, fluid type, pressure, porosity, and lithology. Velocity differences by themselves do not necessarily imply pressure differences. In the present example, we have applied the method to the same stratigraphic unit. Thus, variations associated with lithology can be neglected in principle. The method can be useful as an inversion (prediction) technique in these situations. When many unknowns are present (saturation, fluid type, lithology), the method can be used as a modeling technique.

We have neglected velocity dispersion, which is not easy to take into account, since Q-factor measurements are rare and difficult to obtain with enough reliability. When using laboratory data for the calibration, the effect of velocity dispersion can be significant (Pham et al., 2002).

ACKNOWLEDGMENTS

This work was financed in part by the European Union as part of the Detection of Overpressure Zones with Seismic and Well Data project and by the Norwegian Research Council under the PetroForsk program (N.H.P.). We are grateful to Alpana Bhatt (Norwegian University of Science and Technology) for providing porosity, clay content, and saturation data from logs using her neural-network algorithms, to Stein-Erik Kristensen (Norsk Hydro) for help in seismic interpretation, and to Bruce Hart for a detailed review and useful suggestions.

REFERENCES

Audet, D. M., 1996, Compaction and overpressuring in Pleistocene sediments on the Lousiana shelf, Gulf of Mexico: Marine Petr. Geol., **13**, 467–474.

Belotti, P., and Giacca, D., 1978, Seismic data can detect overpressure in deep drilling: Oil & Gas J., August 21, 76–85.

Berryman, J. G., 1992, Effective stress for transport properties of inhomogeneous porous rock: J. Geophys. Res., **97**, 17409–17424.

Best, M. E., Cant, D. J., Mudford, B. S., and Rees, J. L., 1990, Can velocity inversion help map overpressure zones? Examples from an offshore margin: 60th Ann. Internat. Mtg., Soc. Expl. Geophys., Expanded Abstracts, 763–765.

Bilgeri, D., and Ademeno, E. B., 1982, Predicting abnormally pressured sedimentary rocks: Geophys. Prosp., **30**, 608–621.

Bowers, G. L., 1995, Pore pressure estimation from velocity data—Accounting for overpressure mechanisms besides undercompaction: Internat. Assn. Drill. Cont./Soc. Petr. Eng. Drilling Conf., SPE paper 27488.

Bryant, T. M., 1989, A dual pore pressure detection technique: Internat. Assn. Drill. Cont./Soc. Petr. Eng. Drilling Conf., SPE paper 18714.

Carcione, J. M., 2001, Amplitude variations with offset of pressure-seal reflections: Geophysics, **66**, 283–293.

Carcione, J. M., and Gangi, A., 2000a, Non-equilibrium compaction and abnormal pore-fluid pressures: Effects on seismic attributes: Geophys. Prosp., **48**, 521–537.

———2000b, Gas generation and overpressure: Effects on seismic attributes: Geophysics, **65**, 1769–1779.

Carcione, J. M., and Tinivella, U., 2001, The seismic response to overpressure: A modeling methodology based on laboratory, well and seismic data: Geophys. Prosp., **49**, 523–539.

Carcione, J. M., Gurevich, B., and Cavallini, F., 2000, A generalized Biot-Gassmann model for the acoustic properties of shaley sandstones: Geophys. Prosp., **48**, 539–557.

Childs, C., Manzocchi, T., Nell, P. A. R., Walsh, J. J., Strand, J. A., Heath, A. E., and Lygren, T. H., 2002, Geological implications of a large pressure difference across a small fault in the Viking Graben, *in* Koestler, A. G., and Hunsdale, R., Eds., Hydrocarbon seal quantification: Norweg. Petr. Soc., Special Publ. **11**, 127–139.

Christensen, N. I., and Wang, H. F., 1985, The influence of pore pressure and confining pressure on dynamic elastic properties of Berea Sandstone: Geophysics, **50**, 207–213.

Dutta, N. C., and Levin, F. K., 1990, Geopressure: Soc. Expl. Geophys.

Eaton, B. A., 1972, Graphical method predicts geopressure worldwide: World Oil, **186**, No. 6, 51–56.

Eaton, B. A., and Eaton, T. L., 1997, Fracture gradient prediction for the new generation: World Oil, October, 93–100.

Gangi, A. F., and Carlson, R. L., 1996, An asperity-deformation model for effective pressure: Tectonophysics, **256**, 241–251.

Glennie, K. W., Ed., 1998, Petroleum geology of the North Sea: Blackwell Scientific Publications, Inc.

Goldberg, I., and Gurevich, B., 1998, A semi-empirical velocity-porosity-clay model for petrophysical interpretation of P- and S-velocities: Geophys. Prosp., **46**, 271–285.

Harrold, T. W. D., Swarbick, R. E., and Goulty, N. R., 1999, Pore pressure estimation from mudrock porosities in tertiary basins, Southeast Asia: AAPG Bull., **83**, 1057–1067.

Hart, B. S., Flemings, P. B., and Desphande, A., 1995, Porosity and pressure: Role of compaction disequilibrium in the development of geopressures in a Gulf Coast Pleistocene basin: Geology, **23**, 45–48.

Hashin, Z., and Shtrikman, S., 1963, A variational approach to the elastic behavior of multiphase materials: J. Mech. Phys. Solids, **11**, 127–140.

Helle, H. B., and Bhatt, A., 2002, Fluid saturation from well logs using committee neural networks: Petr. Geosci., **8**, 109–118.

Helle, H. B., Bhatt, A., and Ursin, B., 2001, Porosity and permeability prediction from wireline logs using artificial neural networks—A North Sea case study: Geophys. Prosp., **49**, 431–444.

Holbrook, P., Maggiori, D. A., and Hensley, R., 1995, Real time pore

pressure and fracture pressure determination in all sedimentary lithologies: Form. Eval., December, 215–222.
Kan, T. K., and Sicking, C. J., 1994, Pre-drill geophysical methods for geopressure detection and evaluation in abnormal formation pressures, *in* Fertl, W. H., Chapman, R. E., and Holz, R. F., Eds., Studies in abnormal pressure: Elsevier, 155–186.
Knight, R., and Dvorkin, J., 1992, Seismic and electrical properties of sandstones at low saturations: J. Geophys. Res., **97**, 17425–17432.
Koren, Z., Kosloff, D., Zackhem, U., and Fagin, S., 1998, Velocity model determination by tomography of depth migrated gathers, *in* Fagin, S., Ed., Model-based depth imaging: Soc. Expl. Geophys., Course Note Series **10**, 119–130.
Kosloff, D., Sherwood, J., Koren, Z., Machet, E., and Falkovitz, Y., 1996, Velocity and interface determination by tomography of depth migrated gathers: Geophysics, **61**, 1511–1523.
Krief, M., Garat, J., Stellingwerff, J., and Ventre, J., 1990, A petrophysical interpretation using the velocities of P and S waves (full waveform sonic): The Log Analyst, **31**, 355–369.
Lesso, W. G., Jr., and Burgess, T. M., 1986, Pore pressure and porosity from MWD measurements: Internat. Assn. Drlg Cont./Soc. Petr. Eng. Drilling Conf., SPE paper 14801.
Luo, X., and Vasseur, G., 1996, Geopressuring mechanism of organic matter cracking: Numerical modeling: AAPG Bull., **80**, 856–874.
Mann, D. M., and Mackenzie, A. S., 1990, Prediction of pore fluid pressures in sedimentary basins: Marine Petr. Geol., **7**, 55–65.
Mavko, G., Mukerji, T., and Dvorkin, J., 1998, The rock physics handbook: Tools for seismic analysis in porous media: Cambridge Univ. Press.
Miley, M. P., 1999, Converted modes in subsalt seismic exploration: MS. thesis, Rice Univ.
Miley, M. P., and Kessinger, W. P., 1999, Overpressure prediction using converted mode reflections from base of salt: 60th Ann. Internat. Mtg., Soc. Expl. Geophys., Expanded Abstracts, 880-883.
Pennebaker, E., 1968, Seismic data indicate depth and magnitude of abnormal pressures: World Oil, **166**, No. 7, 73–78.
Pham, N. H., Carcione, J. M., Helle, H. B., and Ursin, B., 2002, Wave velocities and attenuation of shaley sandstone as a function of pore pressure and partial saturation: Geophys. Prosp., **50**, 615–627.
Prasad, M., and Manghnani, M. H., 1997, Effects of pore and differential pressure on compressional wave velocity and quality factor in Berea and Michigan Sandstones: Geophysics, **62**, 1163–1176.
Sayers, C. M., Johnson, G. M., and Denyer, G., 2000, Predrill pore pressure prediction using seismic data: Internat. Assn. Drill. Cont./Soc. Petr. Eng. Drilling Conf., SPE paper 59122.
Traugott, M., 1997, Pore/fracture pressure determinations in deep water: World Oil, August, Deepwater Technology Supplement, 68–70.
Zimmerman, R. W., 1991, Compressibility of sandstones: Elsevier, Science Publ. Co., Inc.